Research Article

Cracking Characteristics and Mechanism of Internal Components of Large-Span Shield Tunnel

Fei Dong,[1] **Ao Li** ![ORCID],[1] **Jun Huang,**[1] **Guang Zhao,**[1] **and Ningwei Chen**[2]

[1]*JSTI Group, Nanjing 210029, China*
[2]*Nanjing Metro Operation Co., Ltd., Nanjing 210046, China*

Correspondence should be addressed to Ao Li; 15115279@bjtu.edu.cn

With the ever-increasing number of large-span shield tunneling projects and the extended operational time, their distinctive internal component issues are becoming more pronounced and exhibiting unique characteristics. In order to reveal the cracking mechanism of concrete on the top of the middle partition wall, based on a large-span shield tunnel section of Nanjing Metro, the crack mode, distribution characteristics, and cracking process of concrete inside tunnel structure were studied by combined field investigation and extended finite element analysis. The results showed that: (1) there were 96 cracks of concrete on the top of the middle partition wall in the interval. Based on the propagation path, number, and shape of cracks, they could be divided into type I, II, III, Y, and Z, with type-Y and type-Z being subtypes of type-I. (2) The crack started at the opposite side of horizontal differential displacement of the flue plate. The development curves of the length and end width of type-I and type-II cracks showed the significant characteristics of three stages. The relationship between crack end width and length was nonlinear, showing that 250 and 225 mm, respectively, were the critical crack lengths growing with the rapid growth of the end width of type-I and type-II cracks. (3) In type-II cracks, the propagation curves of two cracks under the same working condition were consistent, and the spacing of plate joints greatly influenced the length and slope of each stage of the curve. For type-III cracks, the first crack propagation process was basically consistent with type-I and type-II cracks, and the propagation of the other two cracks had obvious brittle characteristics.

1. Introduction

In recent years, with the advancement of technology and equipment manufacturing capacity, the shield tunnel as a highly mechanized and prefabricated method of tunnel construction has been gaining popularity [1]. With the extension of the operational time of shield tunnels, structural damage and diseases have become increasingly prevalent. Many scholars have conducted research on these issues, focusing on water leakage, segment cracking, and detection methods [2]. Leakage water is one of the most common structural diseases of tunnel, and its cause and mechanism are always complex [3]. Gong et al. [4] established the conceptual model to identify sealant behavior of gasketed joint subjected to lateral water pressurization. Du and Tang [5] investigated the failure mechanism of shield tunnels linings considering waterproofing performance

and repercussions of lining joints. Wang and Huang [6] proposed an analytical leakage model to deal with the joint leakage combined with the two-stage characteristics of the joint waterproofing. Based on the purpose of safe and efficient operation, tunnels should be regularly inspected in order to avoid accidents resulting from structure damage. Manual inspection is highly dependent on human subjectivity, and its efficiency is low and the detection coverage is not comprehensive [7]. Thus structural image acquisition and recognition have raised a novel method for shield tunnels detection in recent years [8]. Researchers have proposed various image-based techniques such as castrovision-based change detection [9], automatic crack recognition system [10], and detection of tunnel water leakage based on image acquisition [11].

Above all, the current research on the diseases of shield tunnel mostly focuses on the conventional size shield tunnel
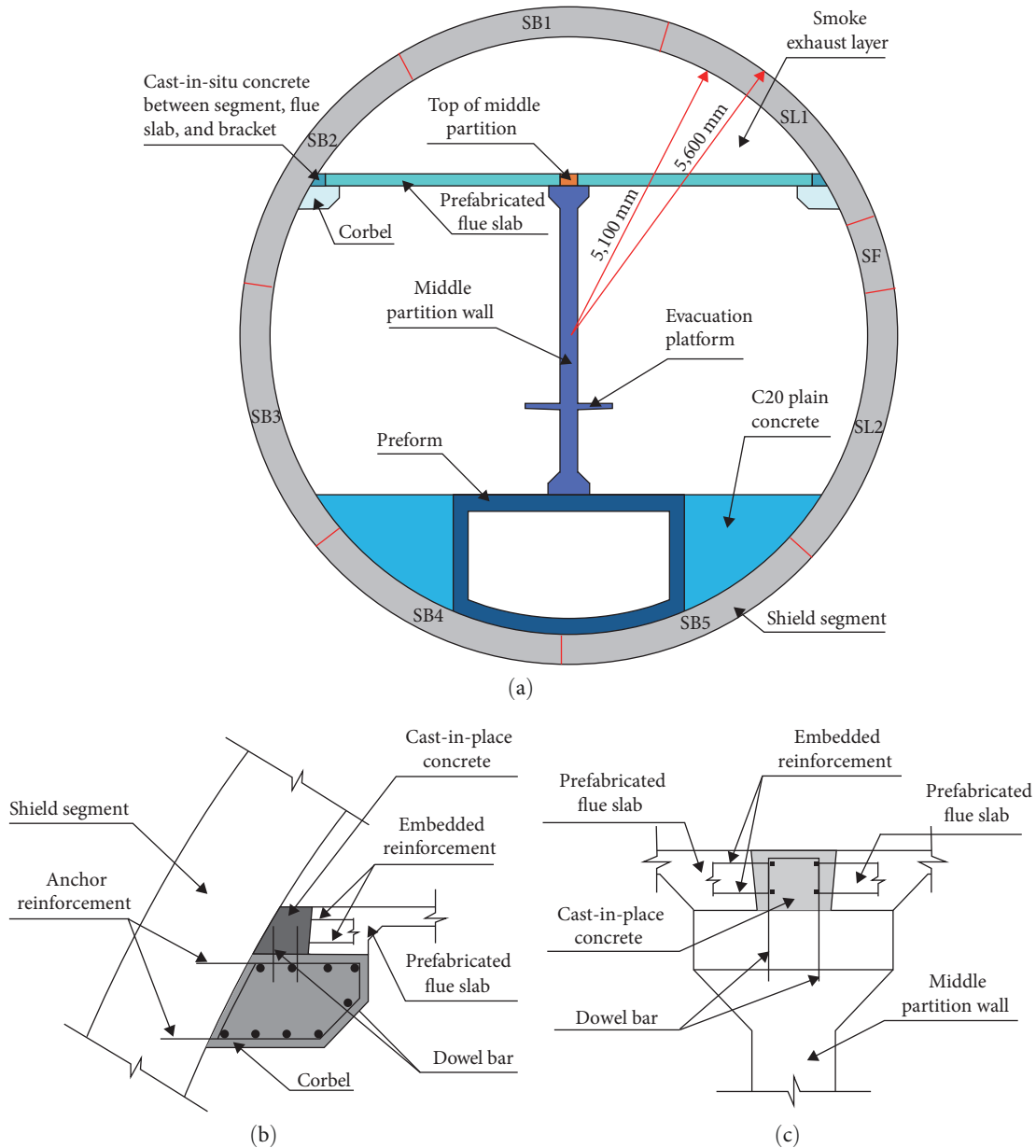
FIGURE 1: Cross-section of a large-span shield tunnel of Nanjing Metro: (a) section of tunnel; (b) connection between prefabricated flue slab and bracket and segment; (c) connection between prefabricated flue slab and middle partition wall.

($D < 10$ m), while the research on the large-span shield tunnel ($D \geq 10$ m) is very few. However, with the increasing demand of tunnel space, large-span shield tunnels have been gradually built, which are used in subway tunnels and underwater highway tunnels. Compared to double-hole small-span shield tunnels, single-hole large-span shield tunnels have the benefits of mitigating engineering risks and reducing costs. Large-span shield tunnels are commonly utilized for constructing six-lane highways or double-track subway tunnels. To improve the space utilization and structural safety of the tunnel, the large-span subway shield tunnel with a single tunnel and double track is equipped with internal structures such as mouthparts, a middle partition wall, and a flue plate. The internal structure is an important part of the large-span shield tunnel. Together with the segments, it forms the

bearing system of the tunnel. Its safety state and durability are essential for the safe operation of vehicles. In the paper, based on the disease investigation of a large-span underwater shield tunnel in Nanjing Metro, the cracking of cast-in-situ concrete on the top of the middle partition wall is investigated, and the cracking mechanism is studied. The research results can provide a reference to the design, operation, and maintenance of large-span shield tunnels.

2. Overview of the Large-Span Shield Tunnel

The typical cross-section of the large-span shield tunnel of Nanjing Metro is shown in Figure 1. It emerges that outer diameter of the shield tunnel is 11.2 m, and thickness and length of each segment are 0.5 and 2 m, respectively. The

segment adopts a general lining ring of C60 concrete, and each segment is composed of one capping block (SF), two adjacent blocks (SL), and five standard blocks (SB). The total length of the shield tunnel is 3.35 km, including 1,677 lining segments. The tunnel structure includes a prefabricated mouth-shaped part, backfill concrete on both sides of the mouth-shaped part, a middle partition wall, an evacuation platform, a flue plate, etc. Except that the mouth-shaped part and flue plate are constructed by factory prefabrication and on-site assembly, other components are cast in situ.

The prefabricated flue plate is 4,040 mm long, 1,600 mm wide, and 200 mm thick. The prefabricated flue plate and middle partition wall are made of C40 concrete, the prefabricated mouth shape is made of C50 concrete, and both sides are backfilled with C20 plain concrete. The load-bearing system is composed of segments, a flue plate, a middle partition wall, and a prefabricated mouth-shaped part that bear the surrounding rock load together. On one hand, the flue plate has to bear the vertical load resulting from dead weight and live load induced by activities such as tunnel inspection and equipment maintenance. On the other hand, the flue plate also bears the horizontal deformation load, which is transferred to the middle partition wall, and could lead to the cracking of the cast-in-situ concrete on the top of the middle partition wall. The field investigation results show that there are many cracks in the concrete at the top of the middle partition wall of the tunnel.

3. Cracking Characteristics of Middle Partition Top

3.1. Crack Types.
The crack on the top of the middle partition wall occurs near the joint of the prefabricated flue plate in two cases: between the joints on both sides and outside the joints on both sides. According to the number of main cracks within the corresponding range of each ring segment, the cracks on the top of the middle partition wall are divided into type-Y, type-Z, type-I, type-II, and type-III (Figure 2). The propagation path of crack type-Y is like the English letter Y, which includes one main crack and two branch cracks. The type-Z crack propagation path goes through two nearly 90° corners, thus forming a stepped crack surface, whose shape is similar to the English letter Z. Type-I, type-II, and type-III cracks have one, two, and three main cracks, respectively, and the cracking surface is plane. There are only six cracks at the position of segment ring seam, and the other cracks are within the segment ring.

3.2. Distribution Characteristics of Cracks.
There are 96 cracks in the concrete on the top of the middle partition wall in the interval tunnel, including 123 cracks, and the crack mode is mainly type-I cracks, accounting for 68.75%, followed by type-II cracks, accounting for 17.71% (Figure 3). The distribution of crack types along the tunnel is shown in Figure 4, and type-I cracks are widely distributed in the tunnel. Except for the first 400 m of the interval tunnel, the number of type-I cracks is the largest.

3.3. Crack Width and Length.
The crack width is characterized by the measurement results near the longitudinal centerline of the middle partition wall. As shown in Figure 5, the minimum and maximum crack widths are 0.05 and 5.4 mm, respectively, and the median crack width is 1.6 mm. The cracks width between 1.2 and 1.6 mm accounts for the largest proportion and about 55.17% of the cracks are with the width less than 1.6 mm.

As shown in Figure 6, maximum and minimum values of crack length are 490 and 165 mm, respectively, and the median length of crack is 285 mm. The crack length between 240 and 280 mm accounts for the largest proportion. The number of cracks with the length less than 320 mm accounts for 79.66% of the total.

4. Influencing Factors of Cracking on the Top of Middle Partition Wall

4.1. Staggering of Circumferential Seam.
The concrete at the top of the middle partition wall is poured between the two flue plates and the middle partition wall, which plays the role of connecting and fixing the two flue plates. It belongs to a nonbearing structure. The prefabricated flue plate is set on the bracket and the middle partition wall on both sides of the tunnel. Affected by the difference and dislocation of the circumferential joints of adjacent segments, the flue plate will transfer the transverse deformation load to the top of the middle partition wall and make it bear additional load. When the maximum principal stress of the component exceeds the material ultimate strength, it will immediately cause concrete cracking. The crack propagation after structural crack initiation is related to stress intensity factor K and fracture toughness K_C (or energy release rate G and fracture toughness G_C).

In order to analyze the influence of segment circumferential joint staggering on the cracking of concrete at the top of the middle partition wall, relevant research is carried out based on the investigation results of circumferential joint staggering of the tunnel. As shown in Figure 7, five measuring points (P1–P5) are set along the adjacent ring during the investigation. For the cracking of the concrete at the top of the middle partition wall, the circumferential joint staggering at the position of the flue plate (P1, P5) is considered. Along the increasing direction of segment ring number, the amount of circumferential seam dislocation of large ring number segment protruding from small ring number is positive and vice versa.

Figure 8 shows the staggering value of segment circumferential seam at P1 and P5 points, in which the staggering value of segment circumferential seam at P1 point of ring 1,567 reaches 53.59 mm, which is the maximum staggering value of circumferential seam in the section, and type-I cracks appear on the top of the corresponding middle partition wall.

As mentioned above, the deformation load is related to the difference of circumferential seam staggering value at P1 and P5 points of the segment ring. Taking 200 rings as an interval, the mean value of the circumferential joints dislocation at points P1 and P5 is calculated corresponding to the
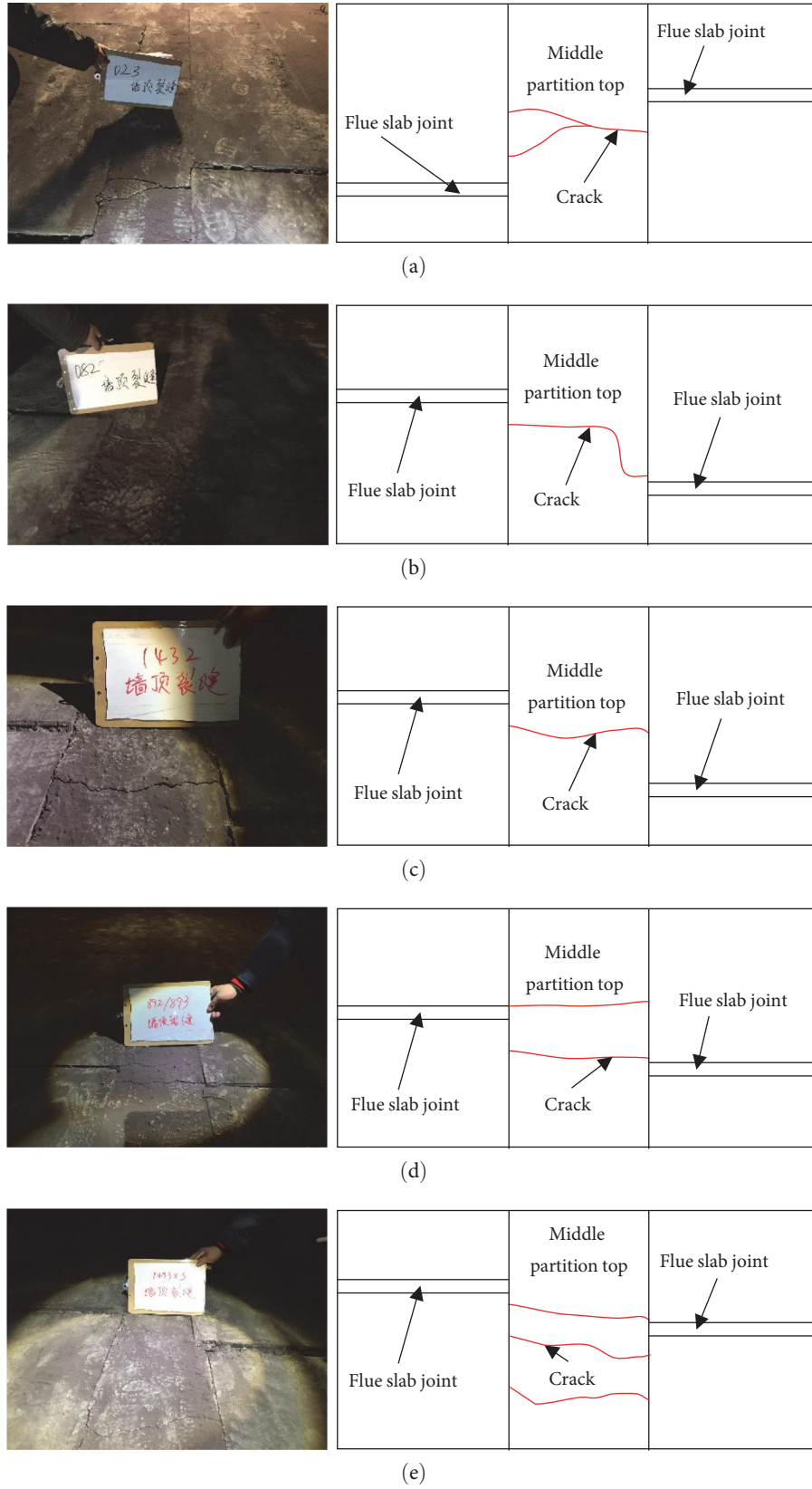
(a)

(b)

(c)

(d)

(e)

FIGURE 2: Crack types at the top of the middle partition wall in the large-span shield tunnel (top view): (a) type-Y; (b) type-Z; (c) type-I; (d) type-II; (e) type-III.
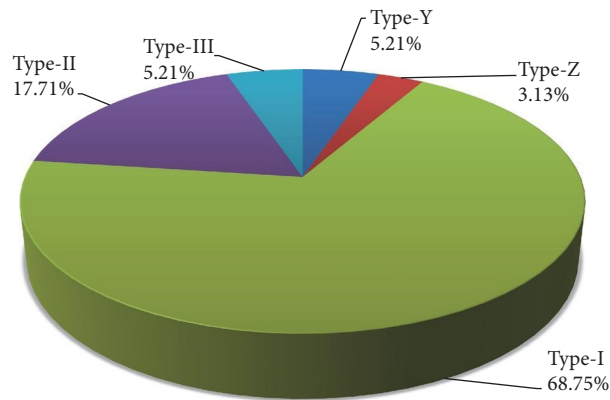
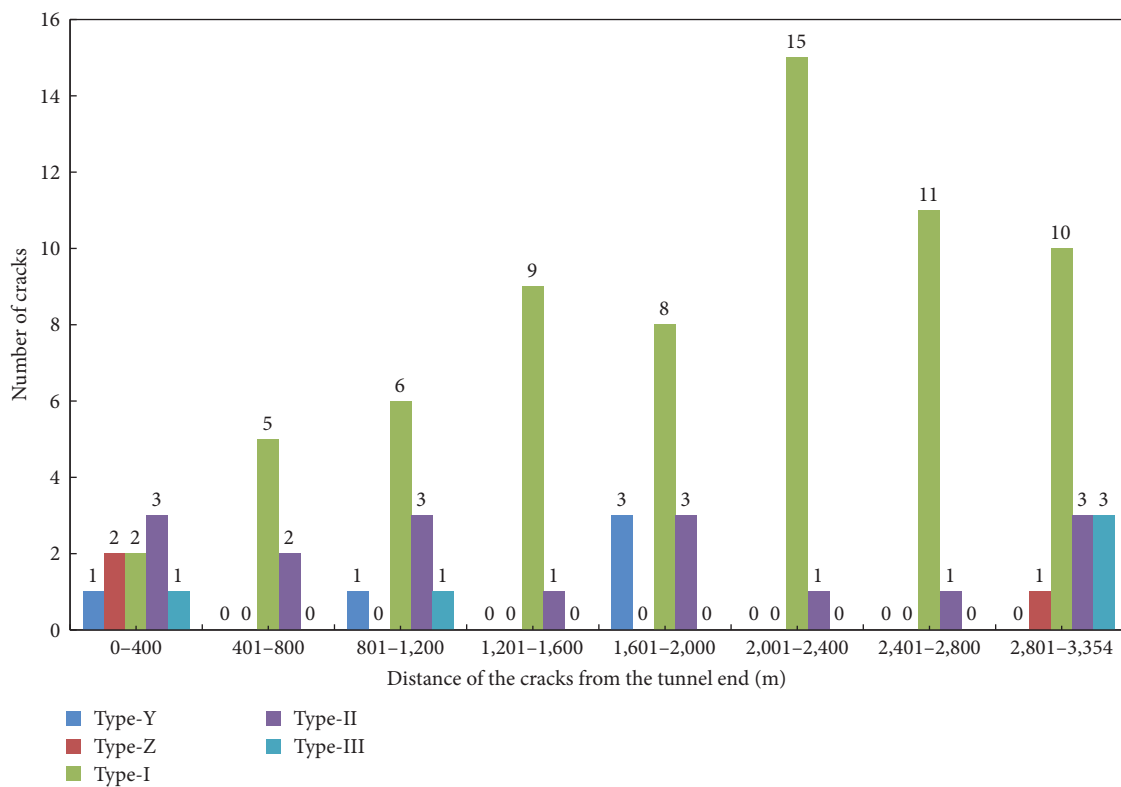FIGURE 3: Distribution of cracks at the top of the middle partition wall in the tunnel.

FIGURE 4: Distribution of crack types at the top of middle partition wall along the longitudinal direction of tunnel.

cracked and uncracked positions of the inner wall top of the interval tunnel, as shown in Figure 9. It can be seen that the calculation results of the amount of circumferential seam staggering in the cracked area are generally larger than that in the uncracked area. Therefore, it can be considered that the cracking of the top concrete of the middle partition wall is related to the staggering amount of the segment circumferential joint at P1 and P5 points.

4.2. Joint Distribution of Prefabricated Flue Plate. As shown in Figure 10, according to the crack trend at the top of the middle partition wall, it can be divided into starting from the plate joint and ending at the plate joint (plate–plate type),

starting from the plate joint and ending at the wall plate joint (plate–wall type), and starting from the wall plate joint and ending at the wall plate joint (wall–wall type), accounting for 3.48%, 30.43%, and 66.09%, respectively. The wall slab joints on both sides near the crack position of the middle partition wall top show apparent local separation (red line, as shown in Figure 10). Therefore, it can be considered that the crack of the middle partition wall top is related to the local deformation load caused by the horizontal differential displacement of the adjacent flue plates on both sides of the joint.

Affected by the plane and vertical alignment of the tunnel, the prefabricated flue plates on both sides of the middle partition wall are not symmetrically arranged in most cases.
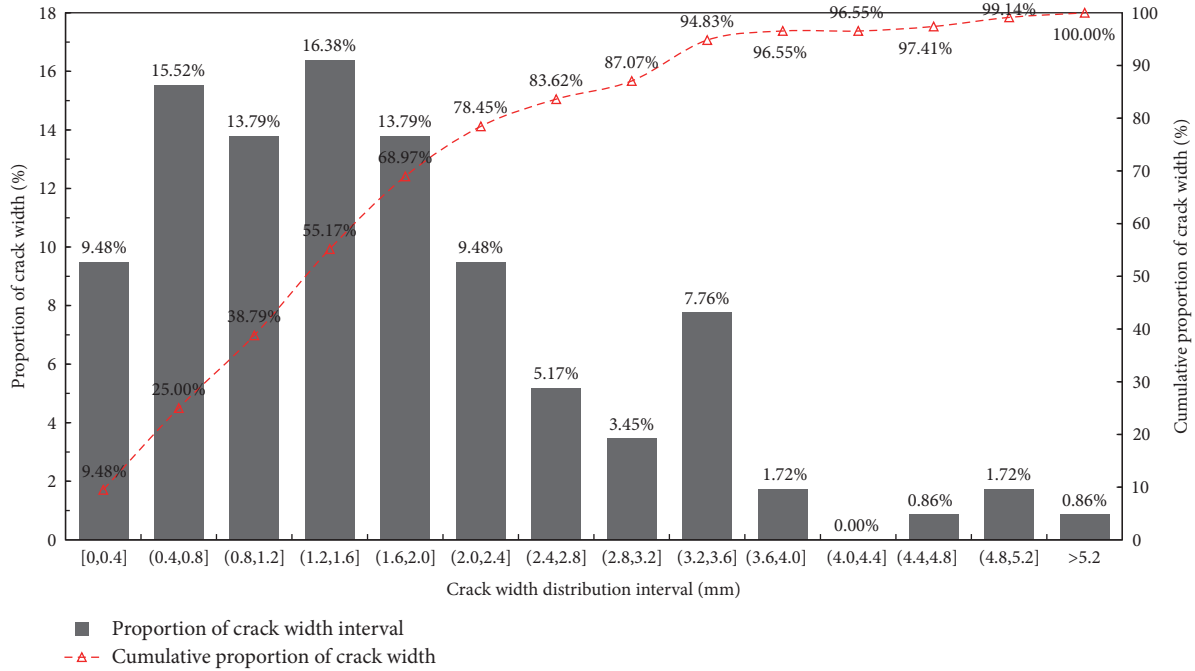
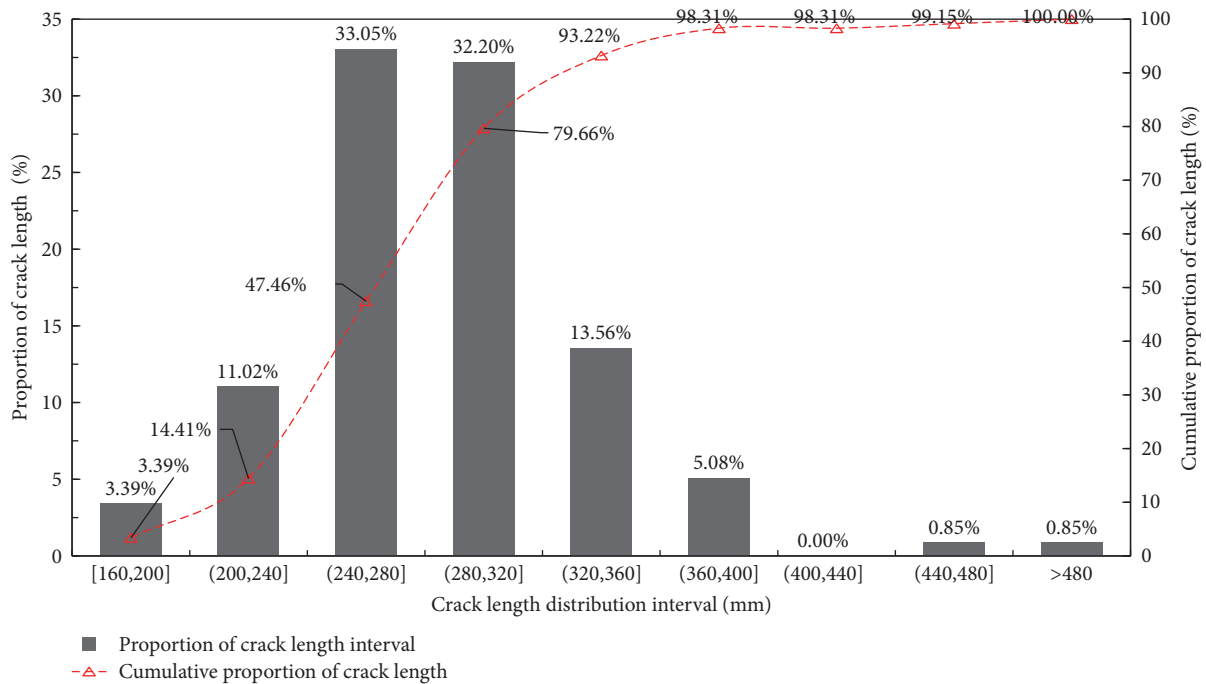FIGURE 5: Statistics of crack width.

FIGURE 6: Statistics of crack length.

Most of the cracks on the top of the middle partition wall appear near the slab joint, and their positions are described by the distance between the two ends of the crack and the slab joint of the flue, as shown in Figure 11. In the figure, d is the width of the flue plate joint, L_1 is the distance between the left end of the crack and the left flue plate joint, L_2 is the distance between the right end of the crack and the right flue

plate joint, and L_3 is the distance between the prefabricated flue plate joints on the left and right sides.

Figure 12 shows the scattered distribution of cracks on the top of the middle partition wall drawn with L_1 as the abscissa and L_2 as the ordinate. The positive and negative values of L_1 and L_2 are shown in Figure 11. The scattered points are relatively concentrated near the diagonals of quadrants 1 and 3, of
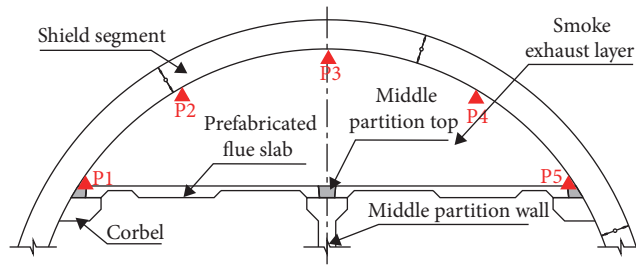
FIGURE 7: Diagram of measuring point position of segment circumferential joint staggering.
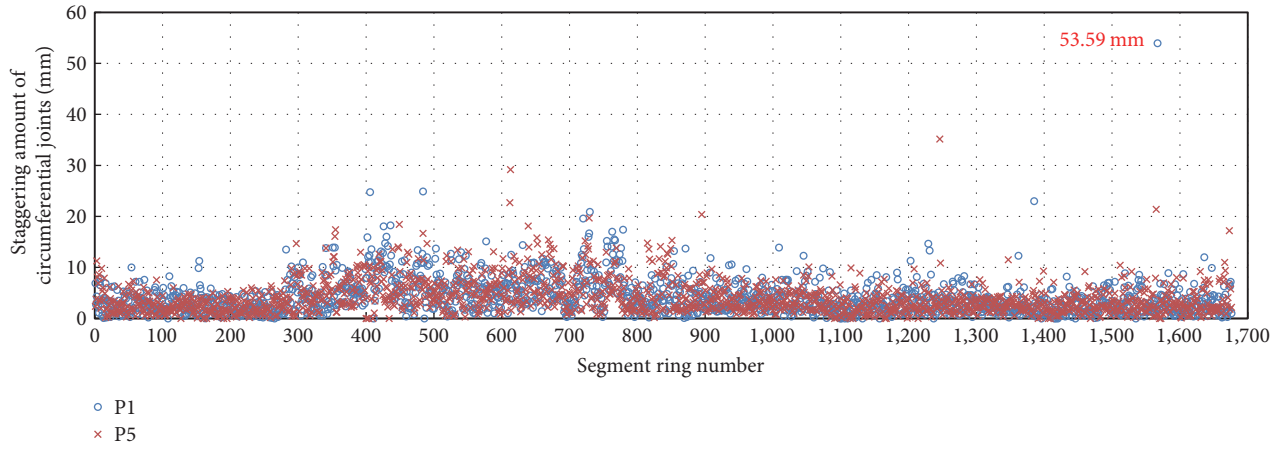

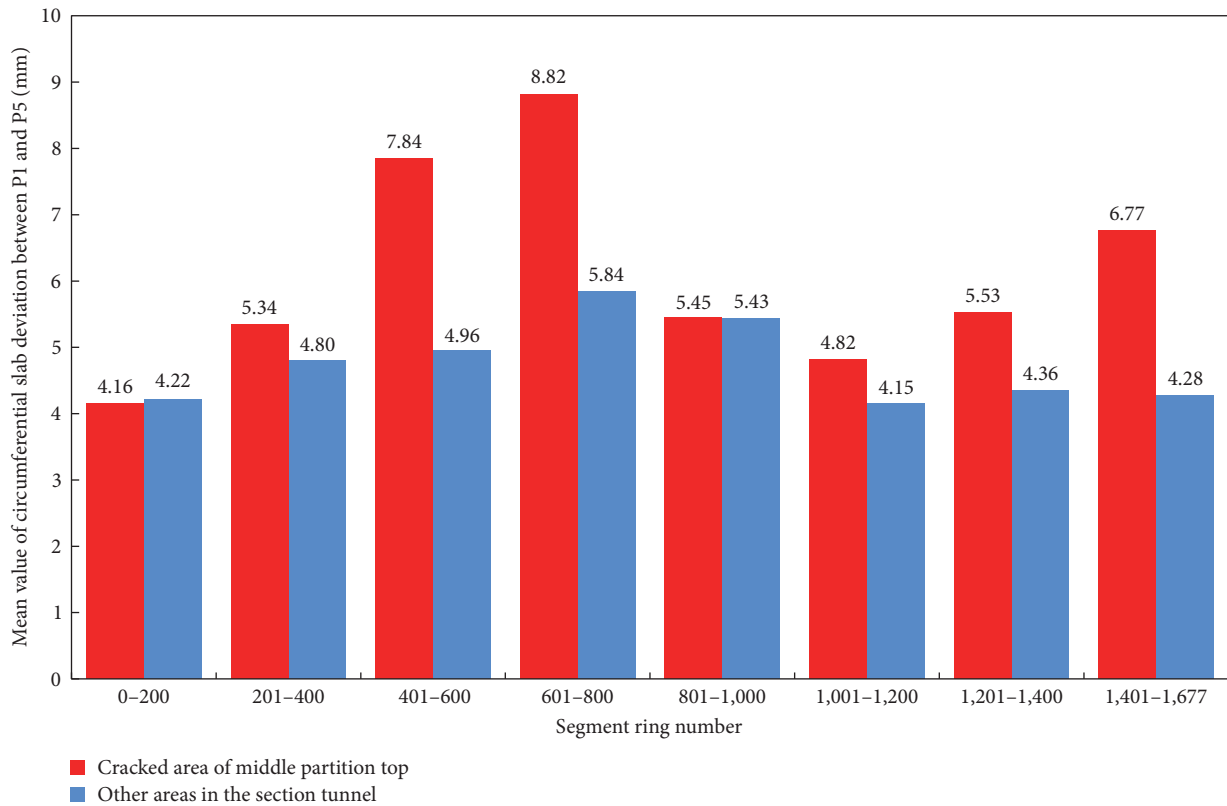FIGURE 8: Staggering amount of segment circumferential joints at P1 and P5 points in the tunnel.

FIGURE 9: Mean difference value of segment circumferential joint between P1 and P5 points.
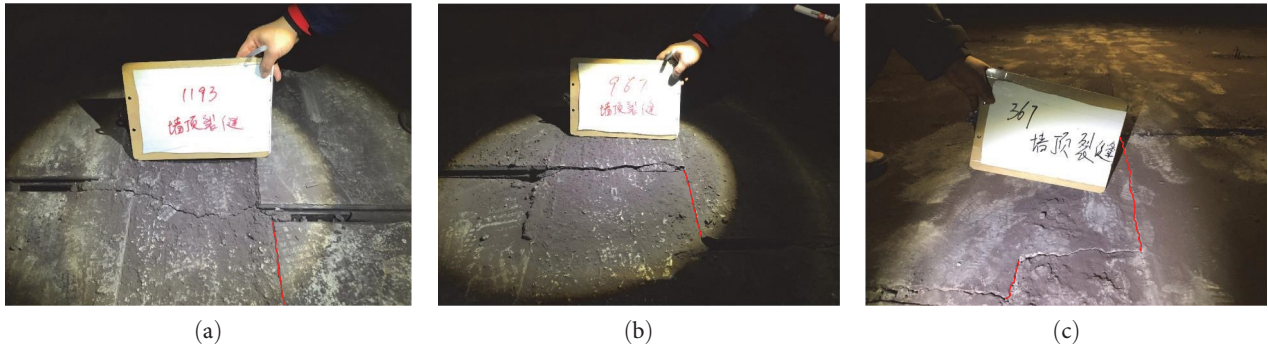
FIGURE 10: Relative position between cracks at the top of middle partition wall: (a) plate–plate type; (b) plate–wall type; (c) wall–wall type.
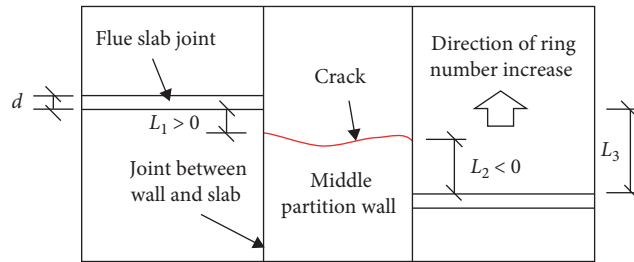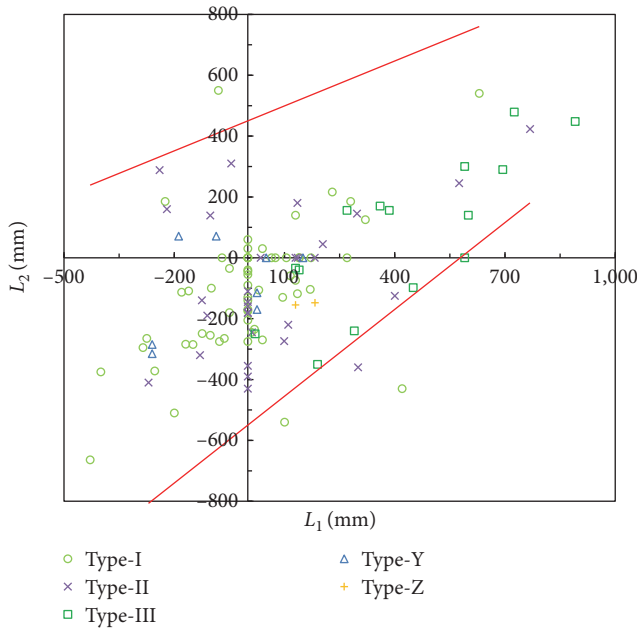

FIGURE 11: Schematic diagram of crack location.

FIGURE 12: Scattered distribution of cracks and slab joints.

FIGURE 13: Finite element analysis model.

which 95.65% of the scattered points of wall top cracks are located between the two dotted lines shown in the figure. Thus, the position of prefabricated flue plate joints has a direct impact on the top cracks of the middle partition wall. Due to the limited number of samples for type-Y and type-Z cracks, which exhibit a certain degree of randomness, analysis was conducted on type I, II, and III cracks with a larger sample size. It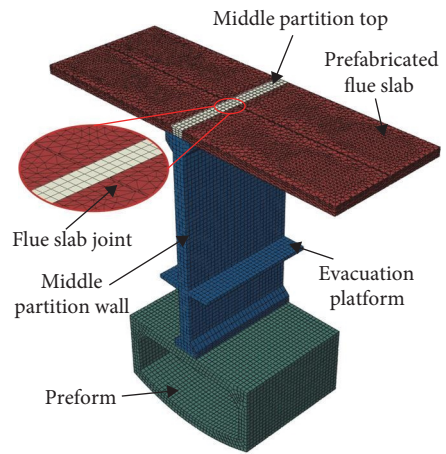 was observed that the scattered distribution of type-I and type-III cracks exhibited good linear correlation, while the scatter points of type-II cracks exhibited nonlinear characteristics.

5. Crack Propagation Mechanism at the Top of Middle Partition Wall

5.1. Numerical Simulation Model. The crack propagation mechanism of concrete on the top of the middle partition wall is studied by extended finite element analysis (XFEM). This paper mainly studies the influence of the horizontal thrust generated by the staggered movement of the prefabricated flue plate on the cracking of the top of the middle partition wall. The numerical simulation model is shown in Figure 13. There is no crack in the prefabricated flue plate,

TABLE 1: Calculation parameters of internal structure.

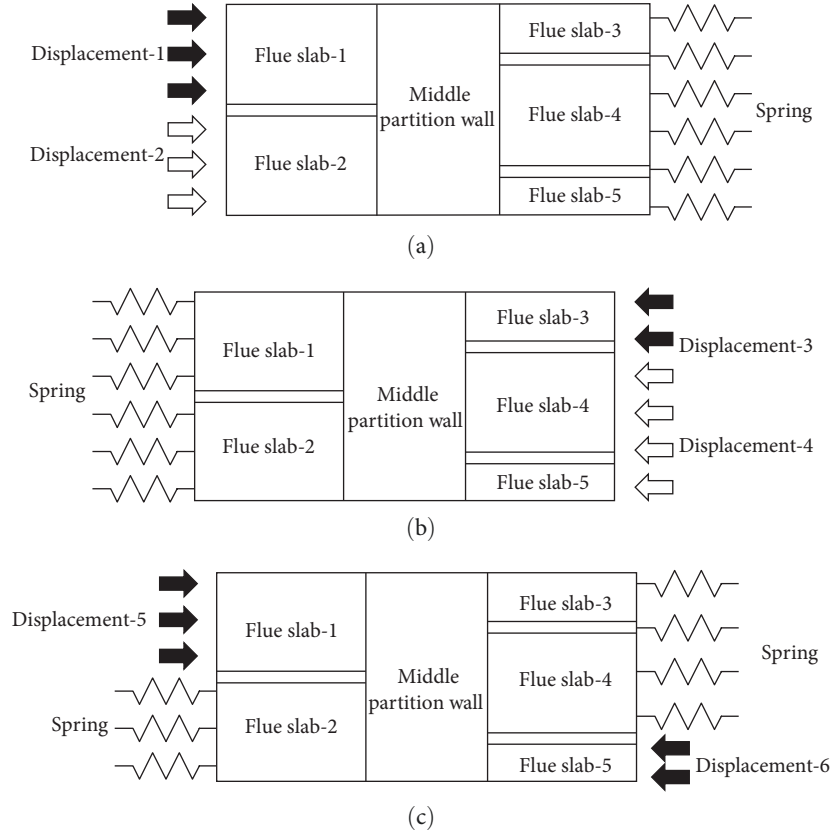| No.	Component	Concrete grade	E (GPa)	Poisson's ratio (v)
1	Prefabricated flue plate	C40	32.5	0.2
2	Middle partition wall	C40	32.5	0.2
3	Mouth-shaped part	C50	34.5	0.2

(a)

(b)

(c)

FIGURE 14: Numerical boundary conditions: (a) differential displacement on the left; (b) differential displacement on the right; (c) differential displacement on both sides.

TABLE 2: Analysis tests.

Boundary condition a	Test	1	2	3	4	5	6	7	8
	$L3$ (mm)	0	100	200	300	400	500	600	700
Boundary condition b	Test	–	9	10	11	12	13	14	15
	$L3$ (mm)	–	100	200	300	400	500	600	700
Boundary condition c	Test	16	17	18	19	20	21	22	23
	$L3$ (mm)	0	100	200	300	400	500	600	700

and the top of the middle partition wall is intact. Only the concrete crack on the top of the middle partition wall is considered in the analysis. The contact relationship between the top of the middle partition wall and the prefabricated flue plate is only compression.

The maximum principal stress cracking criterion based on elastic constitutive law is adopted in numerical simulation, and the linear attenuation evolution rule based on energy is selected. The ideal elastic constitutive model is adopted for other components (Table 1) [12]. The initial crack of the concrete on the top of the middle partition wall is not set, and the maximum principal stress criterion is used to judge the crack initiation and propagation.
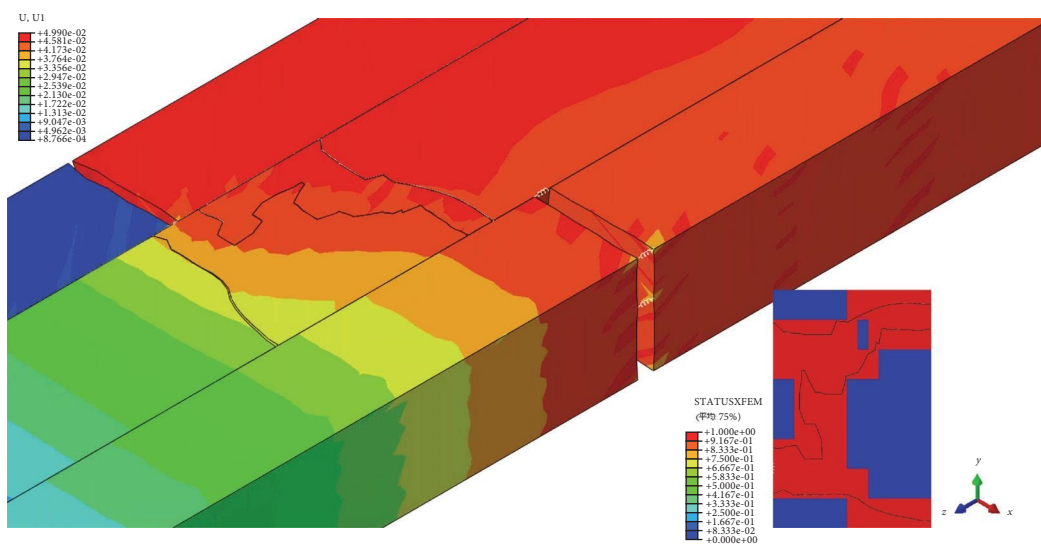
According to the research results of references [13–15], the fracture energy of concrete material at the top of the middle partition wall is calculated as follows:
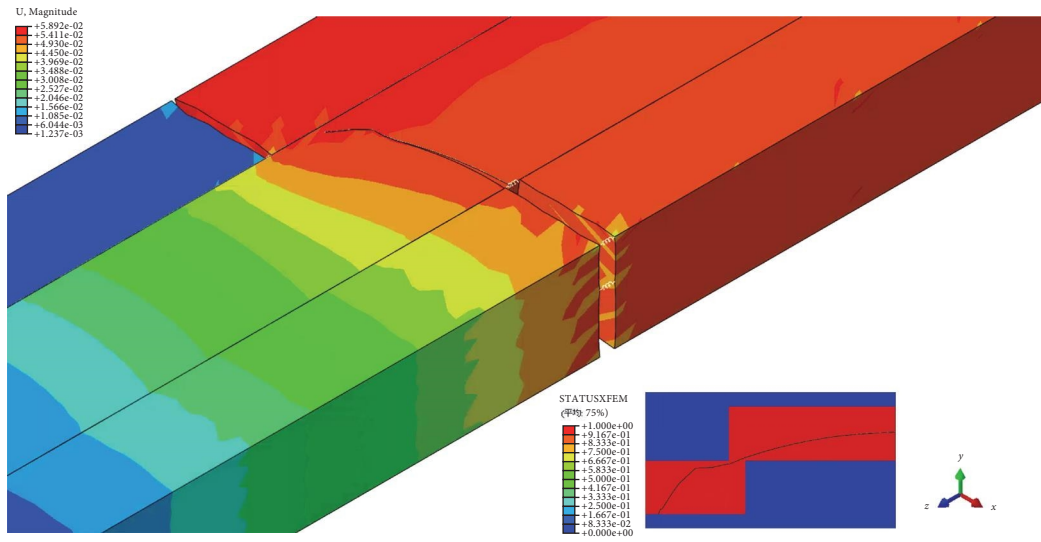
(a)
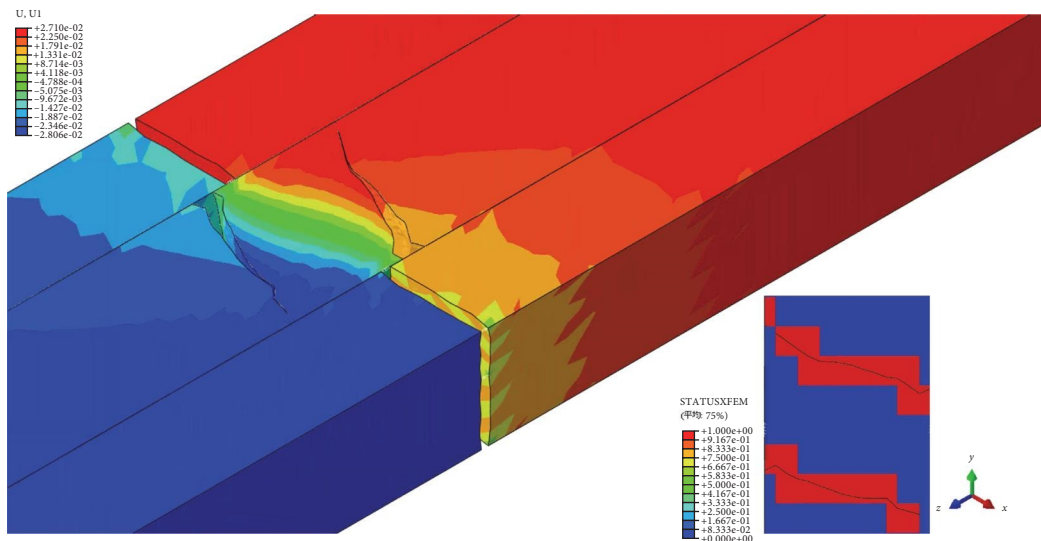
(b)

(c)

FIGURE 15: Cracking types at the top of the middle partition wall (XFEM): (a) type-I crack (test 3); (b) type-II crack (test 16); (c) type-III crack (test 5).
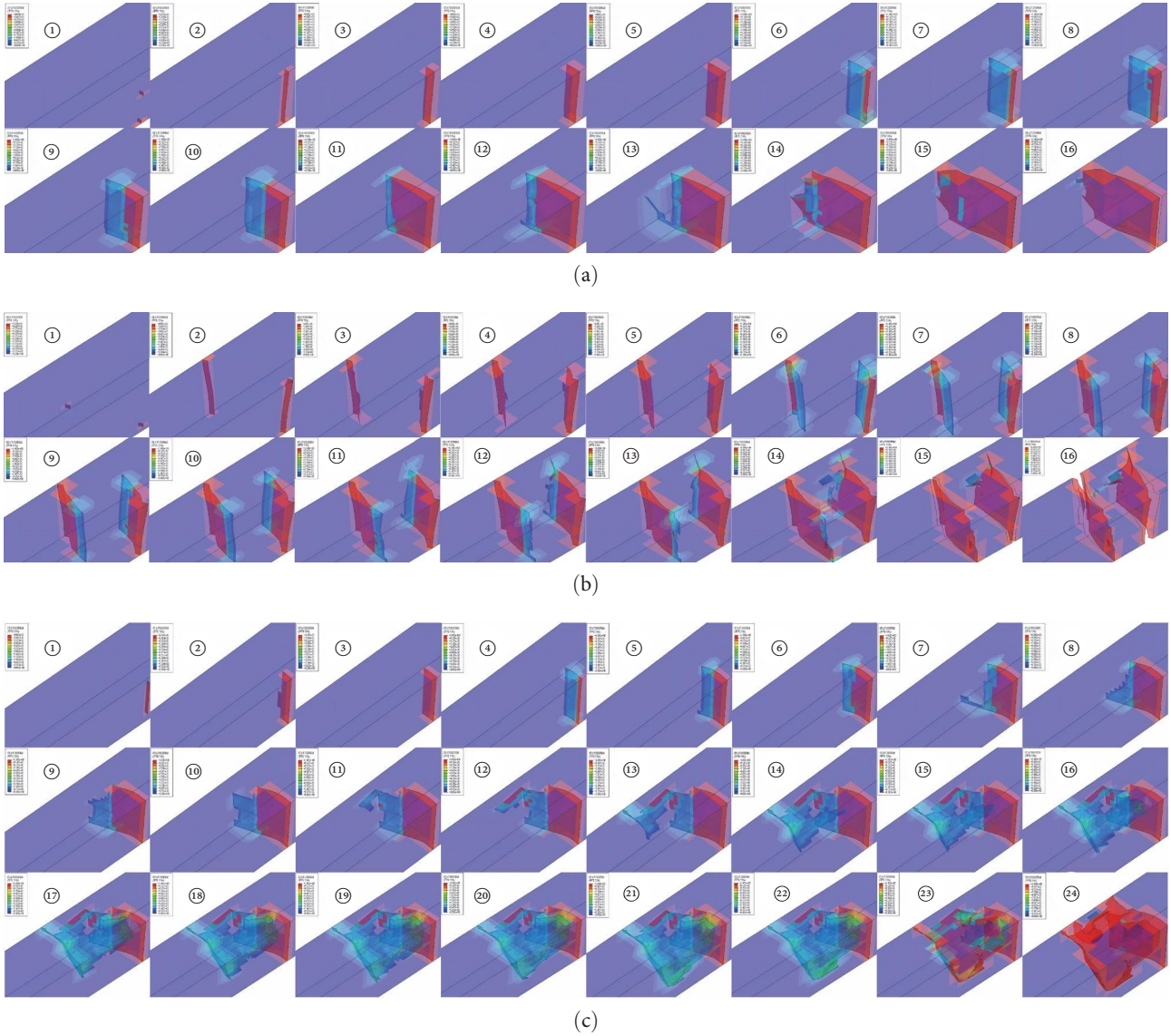
(a)

(b)

(c)

FIGURE 16: Cracking propagation at the top of the middle partition wall (XFEM): (a) type-I crack (test 3); (b) type-II crack (test 16); (c) type-III crack (test 5).

$$G_F = (0.0469d_a^2 - 0.5d_a + 26)\left(\frac{f_c'}{10}\right)^{0.7}, \qquad (1)$$

where G_F is fracture energy per unit area of concrete (Nm/m^2), d_a is the maximum size of concrete aggregate (mm), f_c' is the strength of a concrete cylinder with a size of 150 mm × 300 mm (MPa), and the ratio of its value to the compressive strength of 150 mm cube specimen is 0.81 [16].

The design documents do not mention the concrete's aggregate size on the top of the middle partition wall, which is assumed to be 20 mm in this paper. The concrete grade of the top of the middle partition wall is usually not lower than that of the prefabricated structures on both sides. In this paper, it is considered as C40 concrete. According to Equation (1), the fracture energy is 59.8 Nm/m^2. The ultimate tensile stress of the material is taken as the standard

value of tensile strength (f_{tk} = 2.39 MPa). Based on the site conditions, the joint width of the flue plate is taken as d = 30 mm, and the limiting effect of joint filler on the flue plate is ignored.

As shown in Figure 14, the forced displacement parallel to the horizontal axis of the flue plate is applied to simulate the horizontal action caused by the dislocation of the segment circumferential seam on the top of the middle partition wall. The connecting spring shows the limiting effect of the segment on the horizontal displacement of the flue plate. Considering that the thickness of shield synchronous grouting ring under the influence of stratum loss effect is relatively thin, and its stiffness has limited influence on the stress of structure compared with surrounding rock. The spring stiffness is taken as the subgrade coefficient of the surrounding rock. In the model, fixed boundary conditions are adopted on the bottom and side of the prefabricated mouth shape to
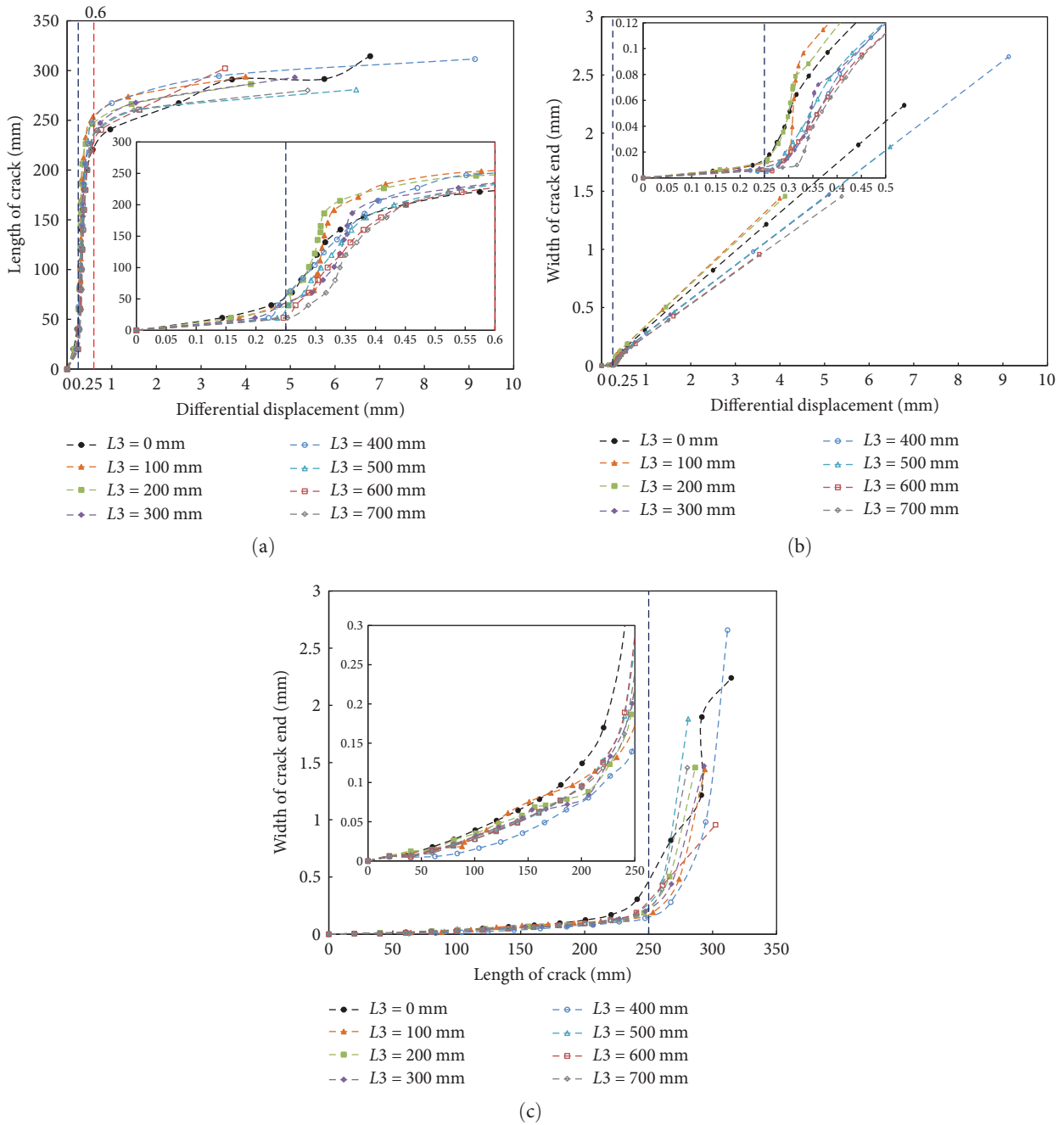
(a)

(b)

(c)

FIGURE 17: Propagation of type-I cracks: (a) relationship between crack length and differential displacement; (b) relationship between crack end width and differential displacement; (c) relationship between crack length and end width.

simulate the limiting effect of concrete filled on both sides and tunnel segments. Based on the field measurement results, 50 mm is selected as the target value of differential displacement between adjacent flue plate joints, and the whole process of cracking and failure of the middle partition top is analyzed.

In addition, the influence of the distance $L3$ between the flue plate joints on the left and right sides on the crack propagation on the top of the middle partition wall should also be considered, as shown in Figure 11. In the analysis, eight cases with $L3$ between 0 and 700 mm are considered, respectively,

and 23 working conditions are considered in combination with displacement boundary conditions (Table 2).

5.2. Analysis of Crack Propagation Mechanism

5.2.1. Crack Type and Propagation Process. Figure 15 shows three crack types calculated based on the above working conditions. The upper left corner shows the overall deformation and crack opening of the structure, and the lower right corner shows the detail of the crack, in which the red part indicates that the unit is completely penetrated by the crack. Except that mode 5 is a type-III crack, the wall top crack
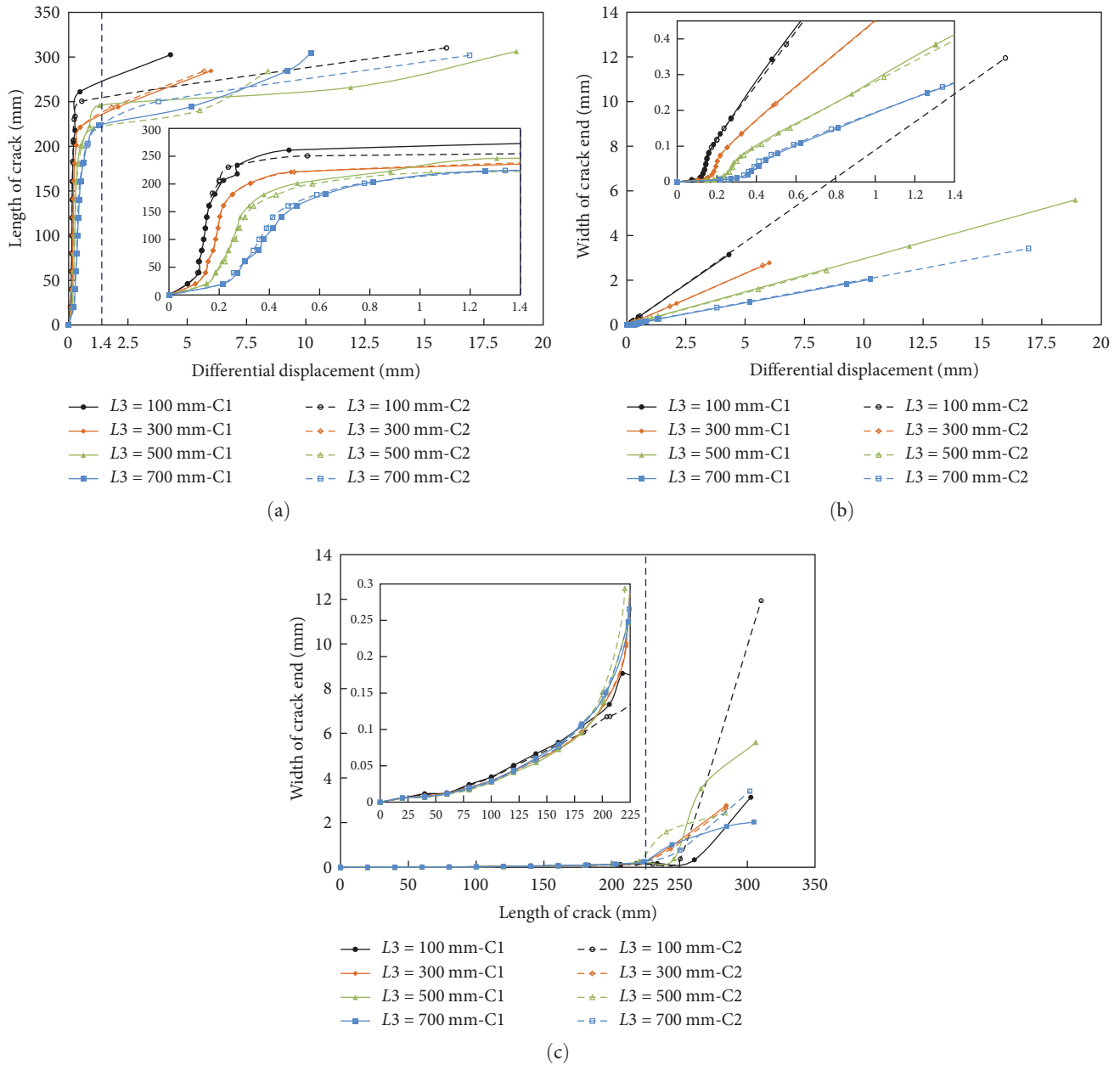
(a)

(b)

(c)

FIGURE 18: Propagation of type-II cracks: (a) relationship between crack length and differential displacement; (b) relationship between crack end width and differential displacement; (c) relationship between crack length and end width.

under the condition of differential displacement on the same side is type-I. Under the condition of differential displacement on both sides, the cracks on the wall top are type-II. Type-Y and type-Z cracks were not obtained by XFEM.

From the microscopic point of view, the hardened concrete is a heterogeneous composite material composed of coarse and fine aggregates, hardened cement paste, and the interface transition zone (ITZ). In the process of crack propagation, complex situations such as aggregates of different sizes, hardened cement slurry, and holes must be randomly distributed at the crack's tip. The basic principle of cracking propagation minimizes energy dissipation [17]. Therefore, it can be considered that type-Y and type-Z cracks are exceptional cases caused by the influence of aggregate or material

defects during the expansion of type-I cracks and are subtypes of type-I cracks. Figure 16 shows the propagation process of type-I, type-II, and type-III cracks as follows:

(1) Type-I crack

The crack starts from the opposite side imposed by the forced displacement, then expands to the side imposed by the forced displacement, and finally runs through the whole cross-section. It expands from right to left in the boundary a and from left to right in boundary b. The fracture surface evolves from the initial plane to the final complex surface.
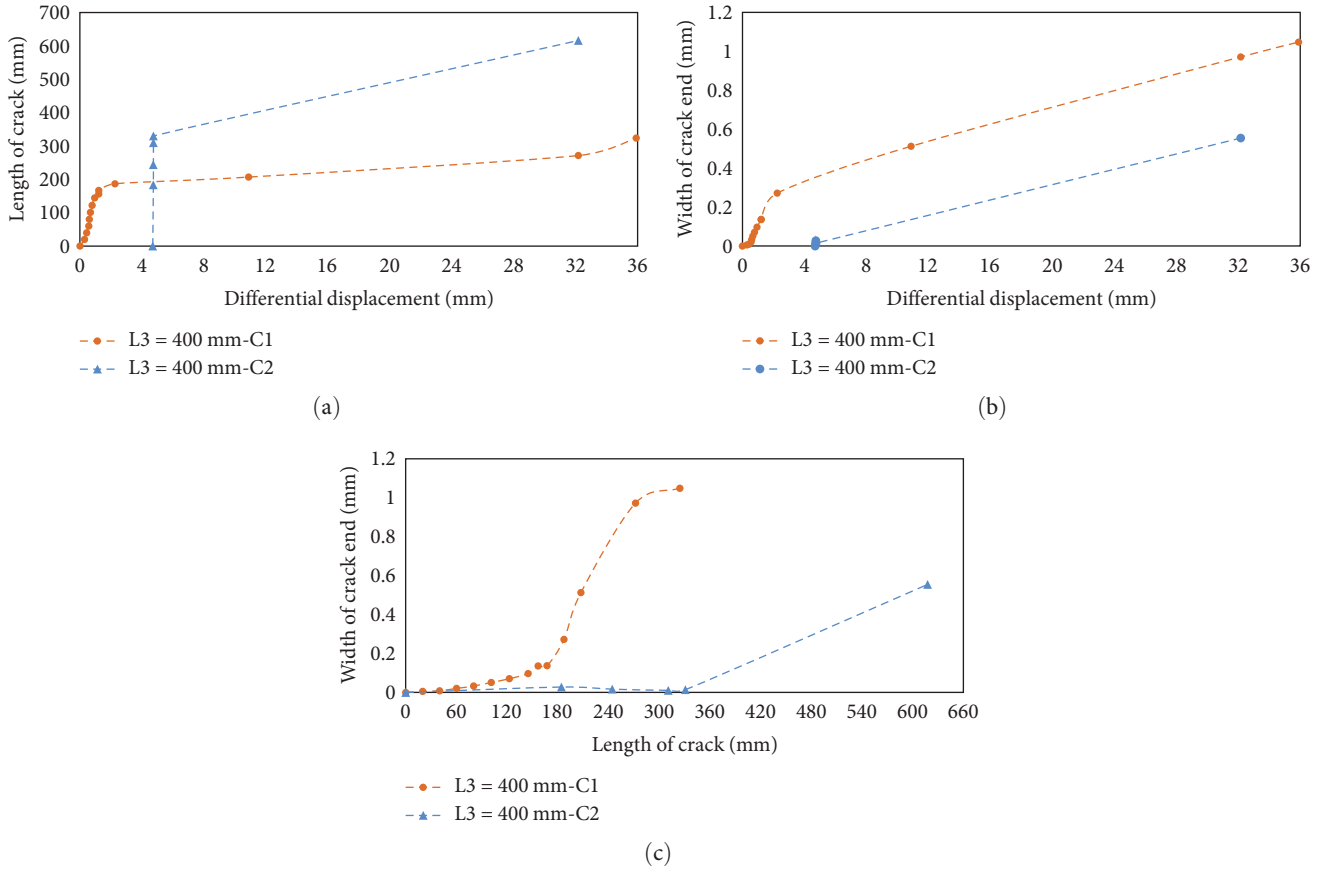
(2) Type-II crack

(a)

(b)

(c)

FIGURE 19: Propagation of type-III cracks: (a) relationship between crack end width and differential displacement; (b) relationship between crack end width and differential displacement; (c) relationship between crack length and end width.

This type mainly occurs in boundary c. Since the forced displacement is applied on both sides simultaneously, the crack starts from both sides simultaneously and finally runs through the whole cross-section. Similarly, the crack surface evolves from the original plane to a complex surface.

(3) Type-III crack

Compared with type-I and type-II cracks, the propagation process of type-III crack is more complex. The wall top concrete cracks near the suitable flue slab joint. After that, the crack expands inside the concrete, and the second crack appears near the joint of the left flue plate. Finally, the third crack appears between the first two cracks, and finally forms a complex crack surface. The propagation process of the latter two cracks has prominent brittle characteristics.

5.2.2. Crack Propagation Mechanism. The relationship curves between the crack length, end width, and the differential displacement on both sides of the prefabricated flue plate crack and the relationship between the crack length and end width are shown in Figures 17–19. Each curve only shows the data related to the crack propagation process (until the crack on the wall top surface penetrates).

(1) Type-I crack

As shown in Figure 17(a), the crack length in each working condition shows three stages, including slow growth, rapid growth, and steady growth with the increase of differential displacement, of which the second stage is the main stage of crack length growth. In the first stage, the relationship between them is nonlinear. In the second stage, the crack completed about 78.3% of the propagation length, and there was an apparent nonlinear relationship between the crack length and displacement. In the third stage, the increase of differential displacement accounts for more than 90% of the total, and the crack propagation length accounts for only about 16.7% of the total length. The relationship between the crack end width and differential displacement, as shown in Figure 17(b), also shows three stages: slow linear increase, nonlinear increase, and rapid linear increase. The third stage is the main stage of crack end width increment. The reason is that after the crack expands to a certain length, the concrete near the crack tip and the flue plate squeezes, and the restraint effect on the wall top concrete tends to be obvious, and near the end of the crack, the two cracks are separated, and the restraint effect is reduced. There is a significant nonlinear relationship between crack length and end width. The increase of crack end width mainly occurs after the differential displacement reaches 250 mm, as shown in Figure 17(c).

(2) Type-II crack

The expansion data of two cracks under the boundary condition of differential displacement on both sides are drawn on the same curve, and the same color represents two cracks in the same working condition. A solid line represents the C1 crack, and the C2 crack is represented by a dotted line, where C1 is the right crack, as shown in Figure 18(b). As shown in Figure 18(a), the propagation of type-II crack is divided into three stages, and the propagation curves of two cracks in the same working condition in the first two stages are consistent. With the increase of flue plate gap spacing $L3$, the differential displacement value of the second stage gradually increases, and the crack length of the third stage decreases. As shown in Figure 18(b), the change process of crack width can be divided into three stages: slow linear increase, nonlinear increase, and rapid linear increase, and the third stage is the main stage. In the same working condition, the changing trend of the end width of the two cracks is consistent. The slope of the curve in each stage gradually decreases with the increase of $L3$, and the length of the first two stages is longer. The crack end width increases nonlinearly with the increase of crack length (Figure 18(c)). When the crack length is less than 225 mm, the end width increases slowly. Then, the width at the end of the crack increases rapidly, which is the main stage of increasing its width.

(3) Type-III crack

During the propagation of type-III crack, the third crack suddenly penetrates the section when the first crack expands to half, which has obvious brittleness characteristics. Therefore, the propagation process of the third crack is not analyzed in the analysis. As shown in Figure 19, the propagation process of the first crack is similar to that of each crack in the first two types. For the second crack, when the differential displacement reaches 4.7 mm, it starts to crack and expands rapidly in a small displacement increment, and then expands gradually with the increase of differential displacement. In the rapid expansion stage, the width of the crack end is very small, and the width gradually increases in the second stage, but its value is very small, about 0.5 mm.

6. Conclusion and Discussion

Based on the investigation of a large-span underwater shield tunnel in Nanjing Metro, the cracking characteristic of cast-in-situ concrete on the top of the middle partition wall is revealed. Furthermore, the crack propagation mechanism is analyzed using numerical simulation. The research conclusions are as follows:

(1) The crack on the top of the middle partition wall occurs near the joint of the prefabricated flue plate in two cases: between the joints on both sides and outside the joints on both sides. There are 96 cracks in the concrete of the middle partition wall on the top of the interval tunnel, with 123 cracks in total, which

are uniformly distributed along the tunnel's longitudinal direction. Cracks types include type-Y, type-Z, type-I, type-II, and type-III. Among them, type-I crack is the main crack, accounting for 68.75%, and type-Y and type-Z are subtypes of type-I crack.

(2) The concrete cracks on the top of the middle partition wall are caused by differential displacement and finally extend to the whole section. Type-I and type-II fracture surfaces evolve from the initial plane to the final spatial surface; after the type-III crack expands on the surface and inside the concrete, it forms a failure body wrapped by a three-dimensional spiral cracking surface.

(3) For type-I and type-II cracks, the curves of crack length and end width show the different characteristics of the three stages. The second and third stages are the main stages of their growth, respectively. There is a nonlinear relationship between the crack end width and the crack length. The crack length reaches the dividing point of slow growth and rapid growth of the end width under 250 and 225 mm, respectively. For type-II cracks, the propagation curves of the two cracks under the same working condition are consistent, and $L3$ greatly influences the length and slope of each stage of the crack propagation curve.

(4) For type-III cracks, the propagation process of the first crack is the same as that of type-I and type-II cracks, and the propagation process of the latter two cracks has prominent brittle characteristics.

Data Availability

The data used to support the findings of this study are included within the article.

Conflicts of Interest

The authors declare that they have no conflicts of interest.

Acknowledgments

References

[1] M. Q. Xiao, "Representative projects and development trend of underwater shield tunnels in China," *Tunnel Construction*, vol. 38, no. 3, pp. 360–367, (in Chinese), 2018.

[2] C. Liu, D. Zhang, and S. Zhang, "Characteristics and treatment measures of lining damages: a case study on a mountain tunnel," *Engineering Failure Analysis*, vol. 128, Article ID 105595, 2021.

[3] L. Xiong, D. Zhang, and Y. Zhang, "Water leakage image recognition of shield tunnel via learning deep feature

representation," *Journal of Visual Communication and Image Representation*, vol. 71, Article ID 102708, 2020.

[4] C. Gong, W. Ding, K. Soga, and K. M. Mosalam, "Failure mechanism of joint waterproofing in precast segmental tunnel linings," *Tunnelling and Underground Space Technology*, vol. 84, pp. 334–352, 2019.

[5] S. Du and J. Tang, "State-of-the-art review on failure mechanism and waterproofing performance of linings for shield tunnels," *Advances in Civil Engineering*, vol. 2022, Article ID 6104725, 9 pages, 2022.

[6] F. Wang and H. Huang, "Theoretical analysis of the joint leakage in shield tunnel considering the typical deformation mode," *International Journal of Geomechanics*, vol. 20, no. 12, 2020.

[7] Q. Ai, Y. Yuan, S.-L. Shen, H. Wang, and X. Huang, "Investigation on inspection scheduling for the maintenance of tunnel with different degradation modes," *Tunnelling and Underground Space Technology*, vol. 106, Article ID 103589, 2020.

[8] L. Attard, C. J. Debono, G. Valentino, and M. Di Castro, "Tunnel inspection using photogrammetric techniques and image processing: a review," *ISPRS Journal of Photogrammetry and Remote Sensing*, vol. 144, pp. 180–188, 2018.

[9] L. Attard, C. J. Debono, G. Valentino, and M. Di Castro, "Vision-based change detection for inspection of tunnel liners," *Automation in Construction*, vol. 91, pp. 142–154, 2018.

[10] M. Ayaho, A. K. Masa, and B. Eugen, "Automatic crack recognition system for concrete structures using image processing approach," *Asian Journal of Information Technology*, vol. 6, pp. 553–561, 2007.

[11] L. Han, J. Chen, H. Li et al., "Multispectral water leakage detection based on a one-stage anchor-free modality fusion network for metro tunnels," *Automation in Construction*, vol. 140, Article ID 104345, 2022.

[12] UDC, "Code for Design of Concrete Structures: GB 50010-2010," China Architecture Publishing & Media Co., Ltd., Beijing, (in Chinese), 2010.

[13] G. M. Chen, J. G. Teng, and J. F. Chen, "Finite-element modeling of intermediate crack debonding in FRP-plated RC beams," *Journal of Composites for Construction*, vol. 15, no. 3, pp. 339–353, 2011.

[14] Z. P. Bažant and E. Becq-Giraudon, "Statistical prediction of fracture parameters of concrete and implications for choice of testing standard," *Cement and Concrete Research*, vol. 32, no. 4, pp. 529–556, 2002.

[15] Comite Euro-International Du Beton, *CEB-FIP Model Code 1990*, Thomas Telford Service Ltd., London, 1991, 1990.

[16] Y. Q. Xin, "Analysis of compressive strength relationship between concrete cylinder specimen and cube specimen," *China Water Power & Electricification*, vol. 2015, no. 7, (in Chinese), Article ID 59, 2015.

[17] S. L. Xu, *Fracture Mechanics of Concrete*, Science Press, Beijing, (in Chinese), 2011.